
This is an electronic reprint of the original article.
This reprint may differ from the original in pagination and typographic detail.

Pankka, Iida; Ahmed, Muhammad Saboor; Tammela, Joonas; Taskinen, Pekka; Lindberg, Daniel

Investigation of End-of-Life Chrome-Magnesia Refractories Using X-Ray Computed Tomography

Published in:
JOM

DOI:
[10.1007/s11837-024-06826-6](https://doi.org/10.1007/s11837-024-06826-6)

Published: 01/11/2024

Document Version
Publisher's PDF, also known as Version of record

Published under the following license:
CC BY

Please cite the original version:
Pankka, I., Ahmed, M. S., Tammela, J., Taskinen, P., & Lindberg, D. (2024). Investigation of End-of-Life Chrome-Magnesia Refractories Using X-Ray Computed Tomography. *JOM*, 76(11), 6650-6659.
<https://doi.org/10.1007/s11837-024-06826-6>

This material is protected by copyright and other intellectual property rights, and duplication or sale of all or part of any of the repository collections is not permitted, except that material may be duplicated by you for your research use or educational purposes in electronic or print form. You must obtain permission for any other use. Electronic or print copies may not be offered, whether for sale or otherwise to anyone who is not an authorised user.



TECHNICAL ARTICLE

Investigation of End-of-Life Chrome-Magnesia Refractories Using X-Ray Computed Tomography

IIDA PANKKA ^{1,3} MUHAMMAD SABOOR AHMED,¹
JOONAS TAMMELA,² PEKKA TASKINEN ¹ and DANIEL LINDBERG ¹

1.—Department of Chemical and Metallurgical Engineering, School of Chemical Engineering, Aalto University, P.O. 16100, 00076 Aalto, Espoo, Finland. 2.—Boliden Harjavalta, Teollisuuskatu 1, 29800 Harjavalta, Finland. 3.—e-mail: iida.pankka@aalto.fi

The lifespan of refractory linings is a major industrial concern for safety, on-line availability, and financial reasons. In copper smelting, batchwise operating matte converters are the furnaces that pose the greatest challenge when it comes to refractory wear and lining life. In this work, the structure and morphology of used magnesia–chrome bricks were studied using X-ray computed tomography and mineralogical techniques. The bricks were taken from various locations of an end-of-life brick lining of an industrial Peirce–Smith converter, after a normal campaign at Boliden Harjavalta smelter (Finland). The results show that it is possible to visualize in 3D, e.g., porosity, metal-containing phases, and refractory magnesia in the used bricks. Different digital images, such as cross-sections and average volume fractions, were used as a non-destructive method to characterize the bricks' internal structure. The metal/matte infiltration in the open porosity was found to differ based on the location in the converter, with some bricks having no metal/matte infiltration and the tuyere line showing metal/matte infiltration at a depth of about 100 mm from the hot face.

INTRODUCTION

Refractory wear in the smelting vessels can be divided into chemical, thermal, and mechanical components.¹ These can appear as a single factor of refractory damage, but, typically, a combination of them determines the refractory lining life, depending on the process intensity, fluxing, and temperature variations of the furnace.² Wear due to chemical dissolution is one of the direct or indirect causes of refractory deterioration and related phenomena, such as densification.^{3,4} Slag and metal/matte penetration is closely related to wear, as it changes the bonding and physical properties of the refractory lining.^{5–7}

It is important to understand how refractory wear occurs, so the consumption of refractories can be lowered as much as the operation conditions allow. There are significant costs associated with

refractories, not just in the form of materials but also as a loss of production due to downtime in relining. In copper smelting, the furnace that possess the greatest challenge in refractory wear is the matte-converting vessel, due to its batchwise operation.^{8,9} In Peirce–Smith converters, the tuyere region and converter mouth are major wear areas,¹⁰ and it is common to carry out partial relining in these zones until a complete relining is needed.^{11,12}

X-ray computed tomography (XCT) is a non-destructive imaging technique based on the change of intensity in the X-rays after penetration. The change in intensity is caused in part of the X-rays getting absorbed, and in part scattered, by the object, affected by the density and the atomic number of the material.¹³ The detector measures the intensity of the X-rays and forms a two-dimensional image based on it. These 2D images are acquired in a multitude of different positions around the axis of rotation of the sample.¹⁴ Software is then used to reconstruct a three-dimensional model of the object based on these two-dimensional images.¹⁵ XCT can be used to provide detailed information on

(Received March 20, 2024; accepted August 5, 2024;
published online September 3, 2024)

a sample's external as well as internal structures. The resolution of the scan is directly proportional to the size of the detector and inversely proportional to the size of the sample.¹⁶

XCT is suited to a variety of applications ranging from medicine to building materials.¹³ It can be used on a multitude of materials, and it can distinguish between phases/domains with different atomic numbers and density. XCT has been conducted in combination with other techniques and conditions, such as the hot metal penetration test,¹⁷ creep testing,¹⁸ acid testing,¹⁹ and water repellents, as well as consolidants.²⁰ XCT studies have been reported on a variety of inorganic materials, including rocks,^{19–22} building materials,^{23,24} and ceramics.²⁵ Some limited XCT studies have even been carried out on refractories, like, e.g., silica,¹⁸ aluminosilicate,²⁶ microporous carbon,¹⁷ and chromia-based materials.²⁷ However, most of the studies have used either unused refractories or laboratory synthesized ceramic samples and more data on actual industrial samples and post mortem cases are needed to better understand the refractory wear.

End-of-life refractories provide traces from the phenomena of its track record, like the bath turbulence, temperature cycling,²⁸ and variable oxygen partial pressure,¹² which are impossible to develop in laboratory circumstances. The operating conditions and converting technologies vary and, therefore, the key phenomena occurring in the linings during operation need many independent observations on the refractory material-converting bath interactions. From technical and scientific points of view, it is important, e.g., to confirm the extend of the crack formation close to the hot-face,⁷ whether it occurs only on the tuyere line or extends throughout the converter. In this work, the morphology and internal structure of used magnesia–chrome refractories from a copper converter were studied using XCT, with the aim of understanding the densification and impregnation phenomena in the linings. In this work, refractory wear was studied in different areas of a Peirce–Smith converter in connection of a large sampling campaign at an industrial copper smelter.

EXPERIMENTAL

Used magnesia–chrome (MC) bricks were taken from the end-of-life brick lining of an industrial Peirce–Smith converter (PSC) at Boliden Harjavalta smelter (Finland) after a 13-week campaign, which is slightly longer than the normal 12-week campaign. Figure 1 shows the locations of the brick samples taken from the converter. Five bricks from different heights (1–5) were taken from the center line C (shown in blue) and three bricks from different heights (1–3) were taken from line W near the right end (shown in green). Sample 1 is above

the tuyere zone, sample 2 is in the tuyere zone, and samples 3–5 are below it. The inside the sampled PSC at Boliden Harjavalta can be seen in Fig. 2.

The converting step uses copper matte from a flash smelting process of about 65% matte grade and it is fluxed with silica in the PSC, as in most copper smelters.²⁹ The smelter uses spent anodes and reverts as coolant during the converting cycles and natural sand as flux.³⁰ Table I shows the remaining brick lengths of the sampled converter bricks compared to the length of an unused brick. The original lengths of the bricks are 45 cm for the tuyere zone and 37.5 cm for the rest. It can be seen in the table that the tuyere zone bricks (2C and 2W) are shorter compared to the bricks right above (1C and 1W) and below (3C and 3W) zone. For the brick length calculations, it was assumed that the 1C and 1W bricks were the same type as the tuyere zone bricks (2C and 2W). The bricks used were of a direct bonded MC quality.

The samples for XCT scanning were drilled with diamond tools from the bricks' hot face towards the cold end. Ethanol was used as coolant during drilling. Due to the limited length of the drill bit, the longer bricks were cut in half before drilling, perpendicular to the hot–cold direction. The drill cores had an average diameter of 12.53 mm with a standard deviation of ± 0.15 mm. The drill cores were sealed in hermetic acrylic tubes after drilling.

XCT measurements were performed for the first 100 mm length from the hot face towards the cold face for each drill core sample using a GE Phoenix vto me lx s 240. A voltage of 150 kV was applied with a current of 100 μ A, which resulted in a power output of 15 W. Each frame had an exposure time of 1000 ms with approximately 10,000 images per scan. The scan was performed in a helical pattern with a 240-kV direct microfocus tube (the smallest voxel size was 5 μ m) in a resolution of 15 μ m utilizing a 0.5-mm Cu filter. To ensure high accuracy, 2 frames from each spot were taken with 0 skip time and averaged. This resulted on average in a total scan time of 5.4 h per brick sample. The XCT data was processed using PerGeos software (Thermo Fisher Scientific, USA), which allowed for the visualization, segmentation, and quantitative analysis of the samples. Due to the similar densities of the copper-containing phases, they were unfortunately not able to be separated using XCT from these samples.

After XCT, the drill core samples were cut perpendicular to the hot–cold direction, forming a series of discs along the brick length. The discs were cast in epoxy, and then ground and polished for mineralogical and chemical analysis of the phases. The samples were carbon-coated for scanning electron microscopy (SEM; Mira 3; Tescan, Brno, Czech Republic) equipped with an UltraDry Silicon Drift Energy Dispersive X-ray Spectrometer (EDS; Thermo Fisher Scientific (Waltham, MA, USA), which was used to perform elemental analyses and

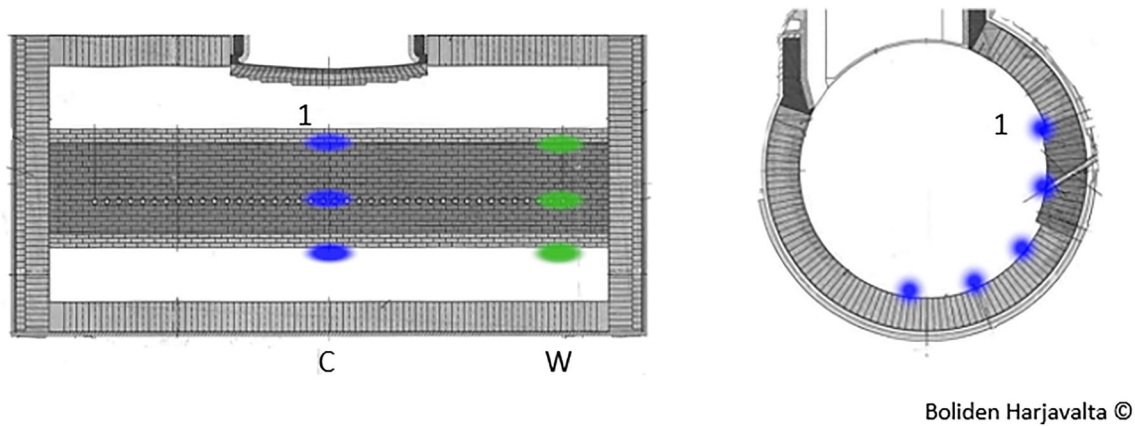


Fig. 1. Locations of the PSC bricks sampled for this study: the C series (5 bricks) from the center line, shown in blue, and the W series (3 bricks) close to the end wall, shown in green (Reprinted with permission from Boliden Harjavalta ©) (Color figure online).



Fig. 2. The inside view of the sampled PSC at Boliden Harjavalta prior to dismantling (Reprinted with permission from Boliden Harjavalta ©).

imaging. An acceleration voltage of 15 kV and beam current of approximately 10 nA on the sample surface were used during the analyses. The elemental compositions of the phases were quantified using the standard materials (refer to online supplementary material Table S-I).

Table I. Remaining lengths of each brick; for brick positions, see Fig. 1

Brick	Remaining length (cm)	Brick	Remaining length (cm)
1C	21	1W	22
2C	17	2W	10
3C	21	3W	15
4C	11		
5C	15		

RESULTS

The bricks exhibited cracks parallel to the hot face in multiple samples. They divided the end-of-life bricks into two or more parts where the shorter part, situated towards the hot face, with a metal-containing phase densified into the magnesia matrix of the MC brick.⁷ Due to temperature variations, a wide crack was formed on the cold side of the densified zone filled with infiltrated copper and matte. These cracks were directly identified from the cuts made for drilling purposes due to their irregular nature compared to the smoothness of the cut surfaces. The residual slag layer on the hot face was also clearly visible. The lower part of the drill core was in many samples and locations in the converter almost unaltered compared with the unused MC brick. Figure 3 shows the 3D XCT image of the sample #2C (on the tuyere line) with the hot face at the top and the segmentation of the MgO phase beside it, in yellow. A large crack is clearly visible separating the sample physically into two parts, with the shorter part towards the hot end.

The obtained 3D X-ray images were manipulated for visualizing selected cross-sections along the length of the brick. An example is shown in Fig. 4 where the contrasts of the matte/metal, MgO particles of the brick, and the porosity have been highlighted in the same 3D graph.

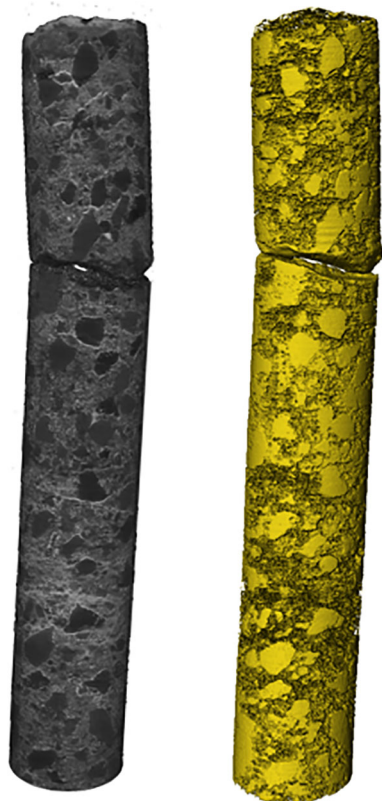


Fig. 3. A 3D model of 2C (center line, tuyere zone) drill core sample with the hot face at the top and its XCT image with the MgO phase segmented in yellow on right. The diameter of the XCT sample is around 12.5 mm (Color figure online).

A similar brick structure was also confirmed in the SEM-EDS measurements. Figure 5 shows the brick structure from three positions along the 2C brick. The metal infiltration into the magnesia matrix is clearly visible. Both copper matte as well as copper metal have infiltrated into the brick as seen in the contrasts of the bright phase. The spinel (MgCr_2O_4) and MgO grains and porosity are clearly visible in the brick structure.

Figure 6 shows selected enlarged cut-out portions along the segmentation of the infiltrated metal-containing phases of the 2C brick with the hot face at the top. It can be seen that the metal/matte penetration is seemingly random, with more metal-containing phases nearer the hot end of the brick than the cold. The metal/matte penetration in the hot face of the brick is visible and its random nature throughout the brick without any preferential texture indicates that it moves through the brick from the bath by surface forces when the oxygen concentration of the blister copper increases during the copper blow (see Fig. 4). Thus, no 'horizontal' movement of the matte/metal, i.e., from the brick joints, can be seen. The characteristics of the copper/matte infiltration obtained in this study confirm the mechanism proposed earlier.^{8,31}

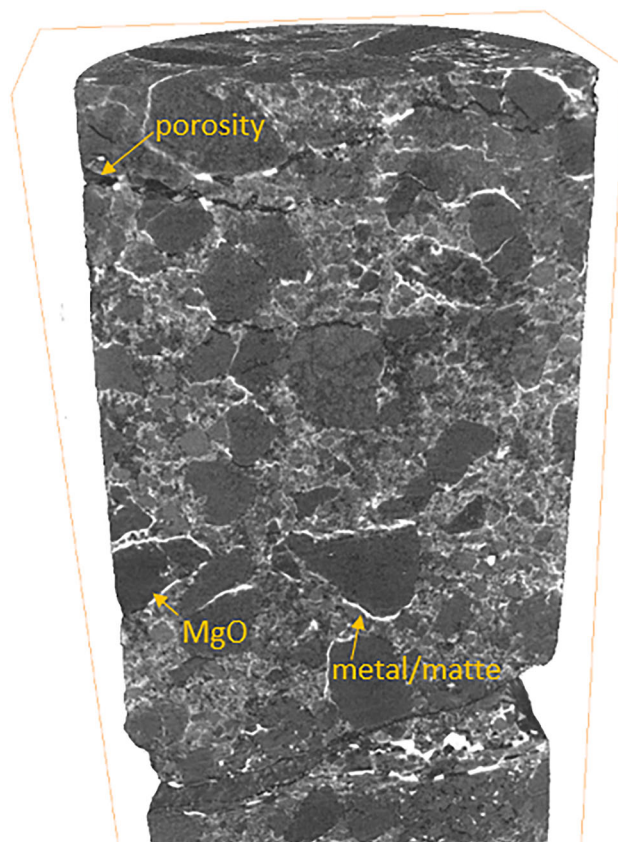


Fig. 4. A digital 3D cross-section of the 2C (converter center line, tuyere zone) sample with a diameter of around 12.5 mm from just below the hot face, showing the XCT contrasts of the different building blocks of the used MC brick and the wide crack separating the 1.5- to 2-cm layer from the mechanically undamaged cold face brick. The diameter of the XCT sample is around 12.5 mm.

The copper/matte infiltration extended to different lengths along the sampled bricks, except in the tuyere zone brick 2C where it was found throughout the imaged brick length of about 100 mm. Also, the porosity of the 2C brick also showed an anomaly in the tuyere zone lining. Figure 7 shows selected enlarged cut-out portions along the porosity segmentation of the 2C brick. The selected enlarged portions are in the same locations as in Fig. 6. A higher thermal load on the tuyere zone from the turbulent flow²⁸ and converting reactions has clustered pores as far as at a 100-mm distance towards the cold end of the bricks.

Not all the brick locations showed metal/matte phase infiltration in XCT. One such brick is the location 4C, a 3D digital cross-section of which is shown in Fig. 8. Other bricks with no visible metal/matte phase infiltration in the XCT were the 3C and 3W bricks. The heterogenous structure of the bricks can be seen from the XCT images, with both the spinel (MgCr_2O_4) and magnesia/periclase (MgO) grains visible (see Fig 8).

SEM analysis show that the pores in the 3C, 4C, and 3W bricks have not been filled by metal/matte infiltration (see Fig. 9, and supplementary Figs. S-1

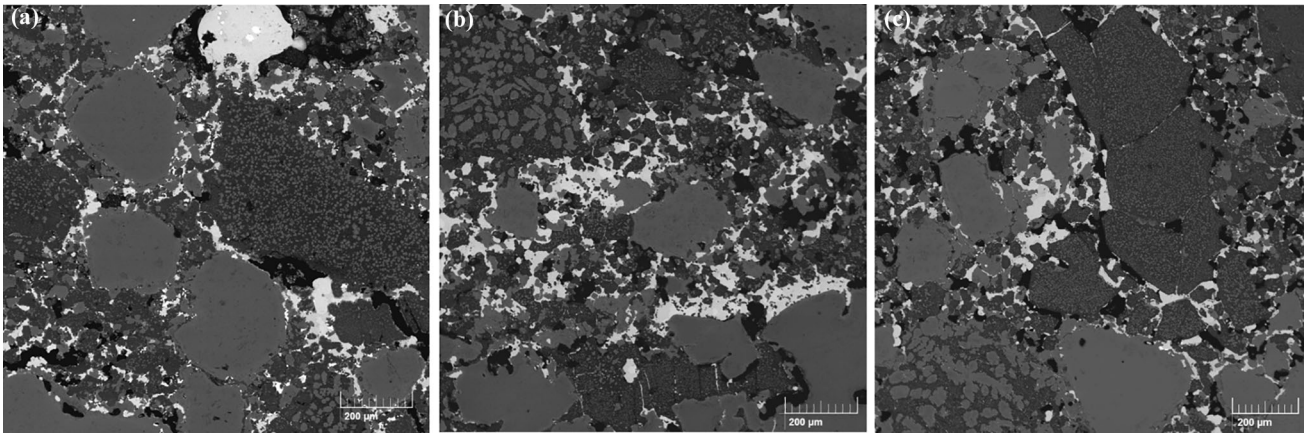


Fig. 5. SEM micrographs from three positions along the 2C (center line, tuyere zone) drill core: (a) 5 mm, (b) 20 mm, and (c) 85 mm from the hot face. The bright white phases are copper, dull white are sulfide matte, light gray are chromite, and dark gray are MgO (Color figure online).

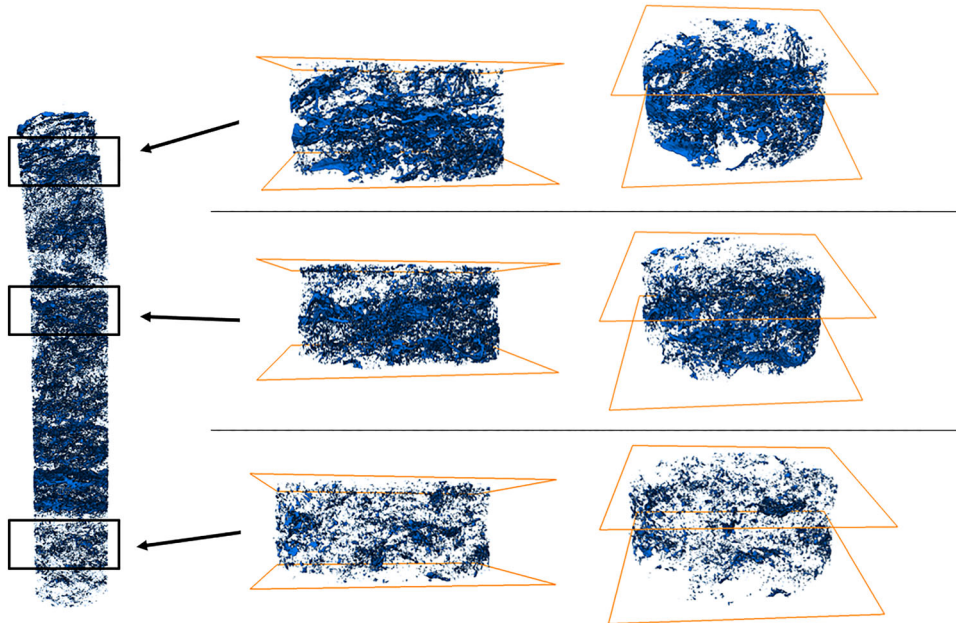


Fig. 6. The 2C brick (center line, tuyere zone) sample and the distribution of its metal-containing phases (copper and matte) showing zoomed-in cuts from three positions along the length of the brick with two inclinations.

and S-2; refer to online supplementary material). When compared to Fig. 5, we can see that samples 3C, 3W, and 4C are lacking the distinctive metal/matte infiltration network visible in other samples. There were some scattered metal/matte particles in the 3C, 4C, and 3W samples (visible as bright spots), but in insignificant amounts.

The metal/matte infiltration in the brick is demonstrated in Figs. 10 and 12 at selected locations of the end-of-life brick lining, and as a function of the distance from the hot face. Figure 10 shows a brick in the bottom of the PSC when the converter is in the blowing condition. Figure 10b shows the average volume fractions of copper + copper matte over each cross-section of the sample core. The infiltration has entered deep in the remaining brick

structure so that the drill core has broken into three parts. It is evident that the observed high-volume fraction of matte/metal, larger than the porosity of the brick, indicates crack formation in the lining where the mechanical strength of the brick has been lost and a metal/matte-filled crack jeopardizes the integrity of the lining. The thickness of the metal/matte 'lens' close to the hot face is also much thicker than in the other locations of the PSC wall lining. A SEM micrograph of this lens, showing it consists of both copper metal and matte, can be seen in Fig. 11.

The locations of the breaks can be seen on the average volume fraction of porosity in Fig. 10c, but the peaks are seemingly low. This can partly be explained by the fact that the cracks along the drill

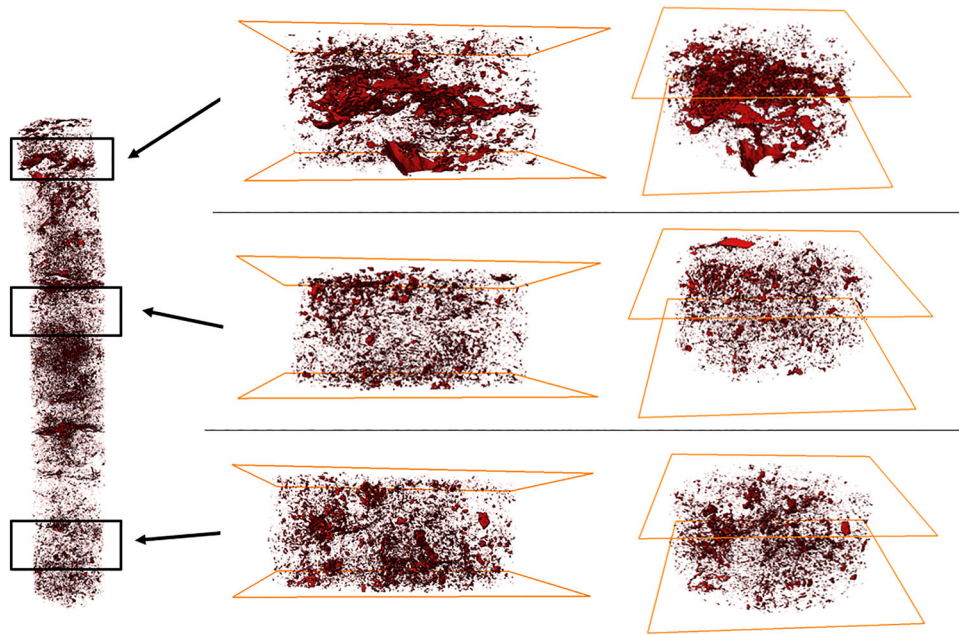


Fig. 7. The 2C (center line, tuyere zone) sample: porosity showing zoom-ins for three positions along the drill core at different distances from the hot face. Note the large pores close to the cold end of the brick showing strong interactions with the converting bath next to the tuyeres, extending to the cold end of the brick XCT scan (big red volumes) (Color figure online).

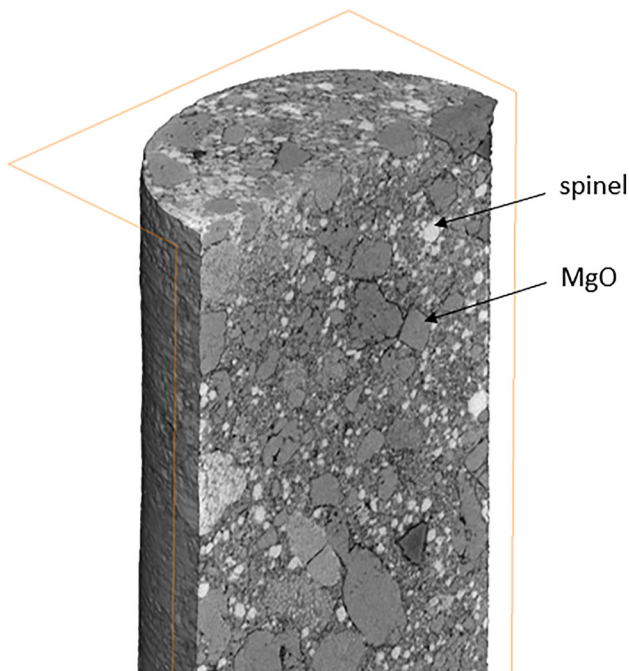


Fig. 8. A digital 3D cross-section of the 4C (center line, below tuyere zone) drill core sample and its spinel ($MgCr_2O_4$) and magnesia (MgO) grains from just below the hot face and its slag layer identified by the X-ray intensity. The diameter of the XCT sample is around 12.5 mm.

core are not perfectly straight and horizontal, which means that parts of the crack or fracture are to a degree present in multiple slices along the drill core. The base porosity value was found to be low compared to the value provided by the

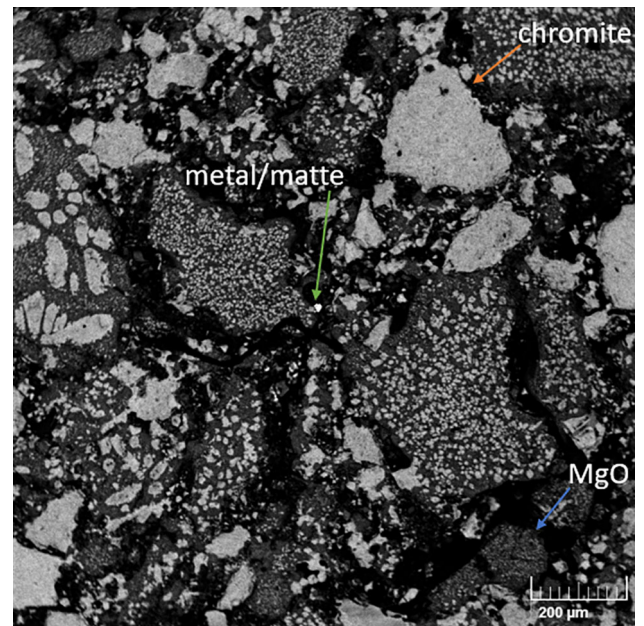


Fig. 9. SEM micrograph of 3W (end line, below tuyere zone) drill core right below the hot face, showing that this brick has not been filled with metal or matte infiltration. The dark gray is MgO, light gray chromite, and bright spots metal/matte (Color figure online).

manufacturer (15–17 vol.%), but this is most likely due to the nature of the XCT measurement. This means that the brick's porosity below the voxel size of the method is not detected. Previous studies have reported difficulties evaluating low porosity, with the error rapidly increasing at smaller length scales than around 200 μm ,^{32,33} and lower porosities have

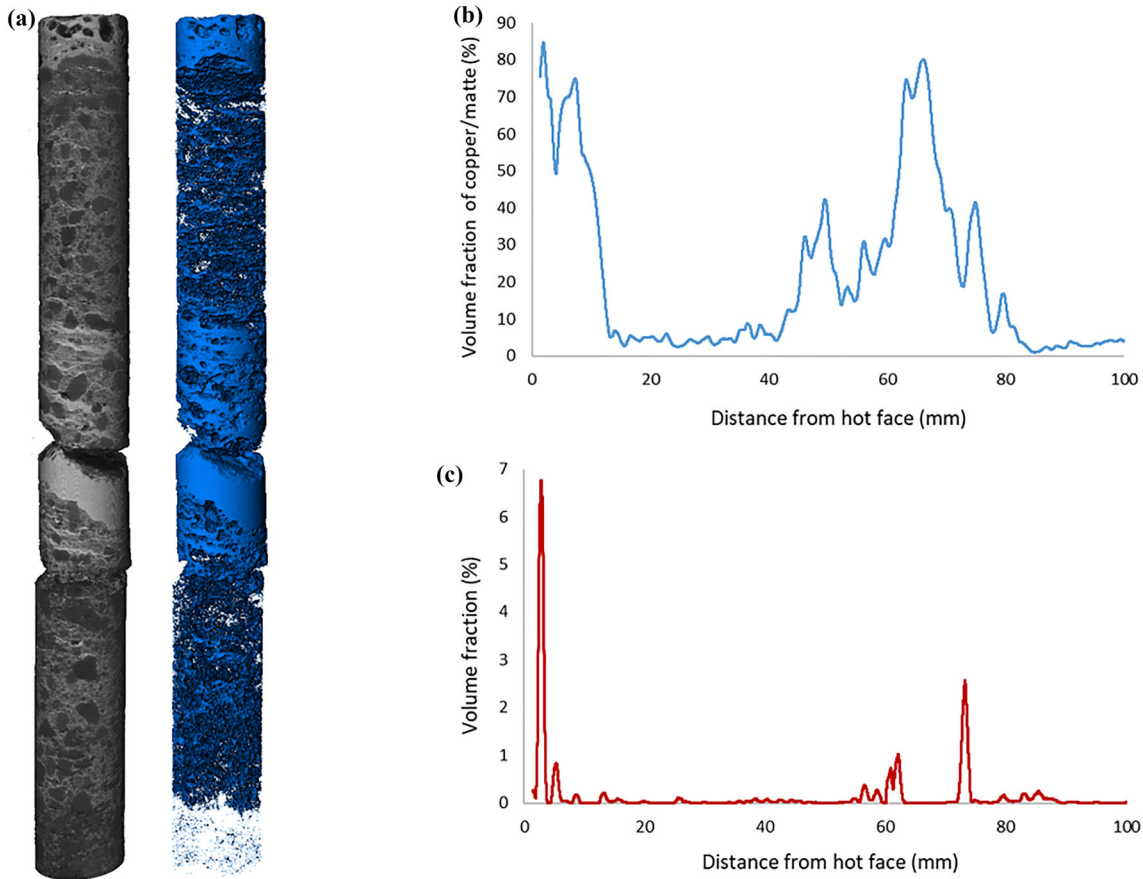


Fig. 10. A 3D scan of the 5C (center line, below tuyere zone) sample with the hot face at the top: (a) the metal/matte-containing phases segmented in blue, and (b) their calculated average volume fraction on each cross-section as a function of distance from the hot face. (c) The calculated average porosity on each cross-section as a function of distance from the hot face; note the abrupt and sharp cold end of the infiltration (Color figure online).

been measured with XCT compared to other methods.¹⁷ This type of low porosity is abundant in the MC refractory samples, as can be seen in Fig. 5. We expect, however, that the trends follow the true porosity of the brick in the XCT data.

Major differences can be seen in metal/matte infiltration along the length of the brick in different parts of the converter. Figure 12 shows the calculated average volume fraction of metal-containing phases on each cross-section as a function of distance from the hot face for the 1C, 1W, 2C, and 2W bricks. The conditions in the bricks on the tuyere level are heaviest due to gas blowing,^{28,34} and infiltration of the copper/matte extends to a length of about 100 mm from the hot face in the converter's centerline on the tuyere level, as shown in Fig. 12b. It looks as if the vicinity of the end wall calms the bath turbulence, and thus reduces the intensity of interactions by the molten matte and metallic

copper with the lining. The infiltration extends only to about 40 mm distance from hot face close to the end wall, as shown in Fig. 12c and d.

Figure 13 shows the volume fraction of metal-containing phases (in blue) and porosity (in red) for bricks #1W and #2W as a function of distance from the hot face. Apart from a spike right by the hot face, the porosity remains close to zero for the length of the metal infiltration and only rises to a volume fraction of 2% at around 40 mm. This indicates a connection between porosity and metal/matte, where the metal/matte phases fill available (open) porosity in the refractory.³⁵ Such a trend was not found in the center line bricks over a distance of 100 mm from the hot face. A similar trend with Fig. 10 can be seen in Fig. 13, where the total measured porosity is too low compared to what has been reported by the manufacturer, most likely due to XCT not measuring fine porosity.

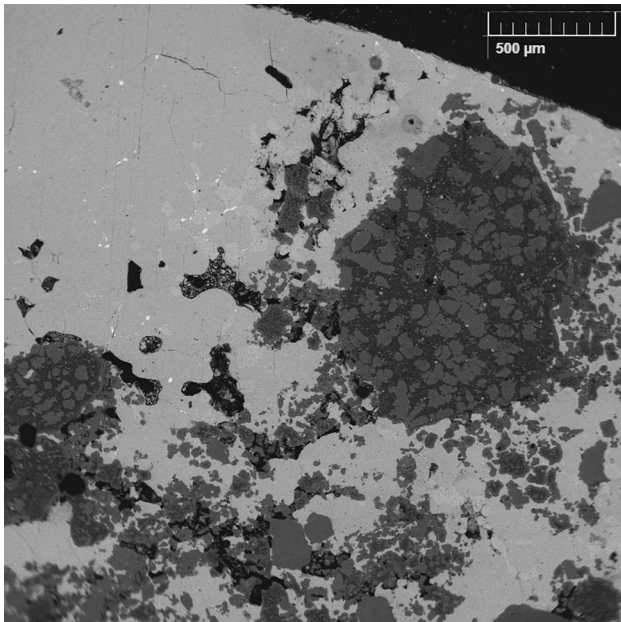


Fig. 11. A SEM micrograph of 5C (center line, below tuyere zone) sample metal lens. The dark gray phase is MgO, middle gray is chromite, very light gray (almost white) is copper matte, white is copper metal, and the bright spots different alloy phases (Color figure online).

CONCLUSION

This study has investigated the microstructures and morphology of used MC bricks from an industrial PSC. The results show that it is possible to segment and obtain quantitative volume fraction data on porosity, metal/matte-containing phases, and magnesia from the XCT scans. Copper metal and copper sulfide matte could, unfortunately, not be separated from each other due to their close densities and the heterogeneous nature of the bricks. That resulted in the inability to decisively point to a large enough location on the drill core sample where only one of the copper-containing phases was present and none of the others. The measured porosities for the bricks were lower than the values provided by the manufacturer, but that is most likely due to the measurement only taking into account porosity above a voxel size and thus excluding fine porosity from the measurement.

The metal/matte infiltration during use in the industrial PSC was found to be random in nature, indicating movements of the liquids to the brick from the bath, evidently through the hot face by surface forces. There were clear differences at different locations of the PSC in the distributions of the metal-containing phases and the depth of

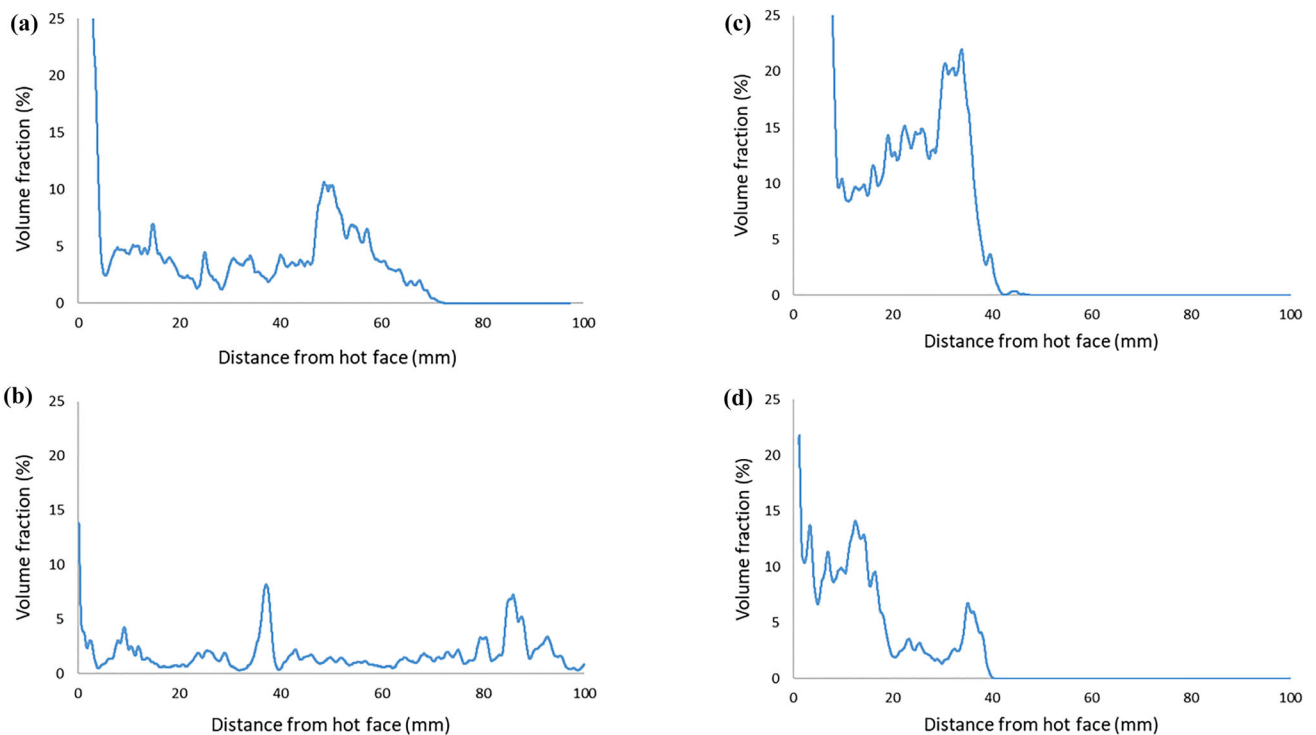


Fig. 12. Calculated average metal/matte containing phase volume fractions on each cross-section as a function of distance from the hot face of each brick: (a) 1C (center line, above tuyere zone), (b) 2C (center line, in tuyere zone), (c) 1W (near end wall, above tuyere zone), and (d) 2W (near end wall, in tuyere zone); the values represent averages over the entire sample cross-section.

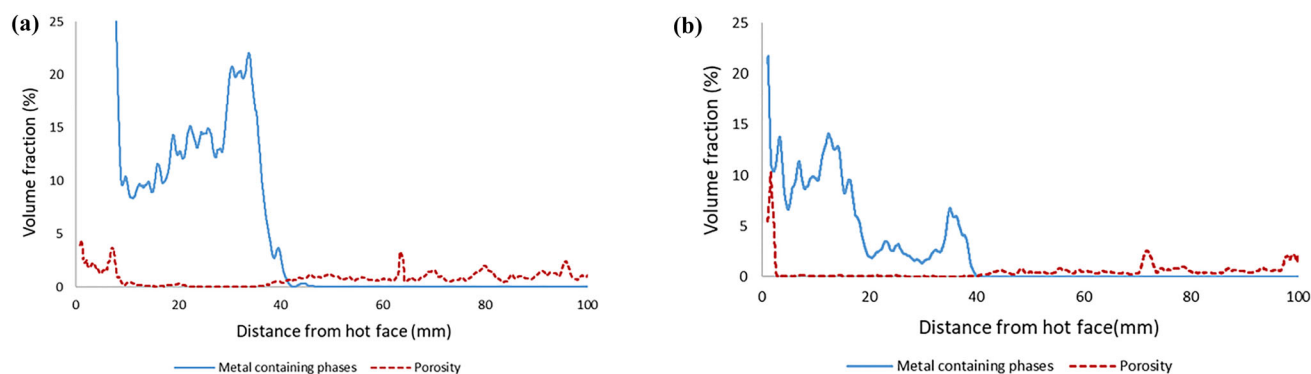


Fig. 13. Calculated average volume fractions of metal containing phases (in blue) and porosity (in red) on each cross-section as a function of distance from the hot face of two near-end wall bricks: (a) 1W (above tuyere zone), and (b) 2W (tuyere zone) (Color figure online).

infiltration. The bricks locating right below the tuyere zone were found to have no metal/matte infiltration at all, while the rest of the bricks showed metal infiltration at varying depths. The depth of the metal/matte infiltration near the end wall of PSC was also found to extend to a shorter distance in the bricks, which is likely due to a less-violent bath turbulence outside the actual tuyere line and above it, as shown by some CFD simulations.

One of the advantages of the XCT method is its non-destructive nature, making it highly suitable to be combined with other methods, such as mineralogical techniques. Also, the ability to view different digital cuts and cross-sections within the brick allows for the study of inside the sample without physically cutting or grinding the sample or separating its phases. Although the brick structure was visible in the 2D and 3D XCT images, further work is needed to obtain more detailed information about the matte/metal infiltration phenomena and to differentiate between the different heavy metal-related phases from the light refractory grains.

SUPPLEMENTARY INFORMATION

The online version contains supplementary material available at <https://doi.org/10.1007/s11837-024-06826-6>.

ACKNOWLEDGEMENTS

Financial support from Boliden is greatly acknowledged. This study utilized the Academy of Finland's RawMatTERS Finland Infrastructure (RAMI) based at Aalto University, GTK and VTT. The work of Dr Jukka Kuva from Geological Survey of Finland in performing the XCT measurements is greatly appreciated. The authors are grateful for Rizky Ananda Fauzi of ITB for drilling the brick samples.

FUNDING

Open Access funding provided by Aalto University.

DATA AVAILABILITY

The raw images from the XCT scans can be found at <https://doi.org/10.23729/cade7ef0-af00-4705-a94a-386e6c9468ed>.

CONFLICT OF INTEREST

Authors declare they have no conflict of interest.

OPEN ACCESS

This article is licensed under a Creative Commons Attribution 4.0 International License, which permits use, sharing, adaptation, distribution and reproduction in any medium or format, as long as you give appropriate credit to the original author(s) and the source, provide a link to the Creative Commons licence, and indicate if changes were made. The images or other third party material in this article are included in the article's Creative Commons licence, unless indicated otherwise in a credit line to the material. If material is not included in the article's Creative Commons licence and your intended use is not permitted by statutory regulation or exceeds the permitted use, you will need to obtain permission directly from the copyright holder. To view a copy of this licence, visit <http://creativecommons.org/licenses/by/4.0/>.

REFERENCES

1. D. Gregurek, A. Ressler, V. Reiter, A. Franzkowiak, A. Spanring, and T. Prietl, *JOM* 65, 1622 <https://doi.org/10.1007/s11837-013-0758-1> (2013).
2. D. Gregurek, C. Majcenovic, A. Spanring, and M. Kirschen, *Wear Phenomena of Basic Brick Lining in the Copper Industry*. In: *Proc. Copper 2013-Nicholas Themelis Symposium on Pyrometallurgy and Process Engineering (Vol III)*, Santiago Chile. ChIMM, Santiago (Chile), 473 (2013).
3. Z. Tao, K. Mukai, H. Yonezawa, and Y. Yoshimura, *J. Tech. Assoc. Refract. Jpn.* 20(1), 10 (2000).

4. C. Goni, M. Barbés, V. Bazán, E. Brandaleze, R. Parra, and L. González, *J. Ceram. Soc. Jpn.* 114, 672 <https://doi.org/10.2109/jcersj.114.672> (2006).
5. K. Mukai, Z. Tao, K. Goto, Z. Li, and T. Takashima, *J. Tech. Assoc. Refract. Jpn.* 21(1), 3 (2001).
6. I. Pérez, I. Moreno-Ventas, and G. Ríos, *Ceram. Int.* 44, 13476 <https://doi.org/10.1016/j.ceramint.2018.04.168> (2018).
7. M. Tikkanen and P. Taskinen, *Int. Ceram. Rev.* 30, 333 (1981).
8. C.A. Rodríguez González, W.F. Caley, and R.A.L. Drew, *Metall. Mater. Trans. B* 38, 167 <https://doi.org/10.1007/s11663-007-9031-8> (2007).
9. X. Hou, D. Ding, G. Xiao, E. Jin, X. Chong, J. Luo, and Y. Gao, *Ceram. Int.* 49, 15395 <https://doi.org/10.1016/j.ceramint.2023.01.124> (2023).
10. D. Gregurek, K. Reinharter, J. Schmidl, and A. Spanring, In: *Proc. 58th Internat. Annual Conf. Metall. II(COM) – Cu 2019*. MetSoc, Montreal. USB Proc., paper #567788 (2019).
11. J.-L. Liow, P. Tsirikis, and N.B. Gray, *Can. Metall. Q.* 37(2), 99 (1997).
12. I. Pérez, I. Moreno-Ventas, and G. Ríos, *Ceram. Int.* 44, 18363 <https://doi.org/10.1016/j.ceramint.2018.07.052> (2018).
13. L. Vásárhelyi, Z. Kónya, Á. Kukovecz, and R. Vajtai, *Mater. Today Adv.* 8, 100084 <https://doi.org/10.1016/j.mtadv.2020.100084> (2020).
14. L. De Chiffre, S. Carmignato, J.-P. Kruth, E. Schmitt, and A. Weckenmann, *CIRP Ann.* 63(2), 655 <https://doi.org/10.1016/j.cirp.2014.05.011> (2014).
15. S. Carmignato, W. Dewulf, and R. Leach, *Industrial X-ray Computed Tomography* (Springer, Switzerland, 2018).
16. J.E. Elkhoury, R. Shankar, and T.S. Ramakrishnan, *Transp. Porous Med.* 129, 413 <https://doi.org/10.1007/s11242-019-01275-1> (2019).
17. J. Stec, J. Tarasiuk, S. Wronski, P. Kubica, J. Tomala, and R. Filipek, *Materials*. 14, 3148 <https://doi.org/10.3390/ma14123148> (2021).
18. J. Fan, Y. Li, Y. Gao, X. Zhang, and P. Jiang, *Ceram. Int.* 47, 18084 <https://doi.org/10.1016/j.ceramint.2021.03.124> (2021).
19. J. Dewanckele, T. De Kock, G. Fronteau, H. Derluyn, P. Vontobel, M. Dierick, L. Van Hoorebeke, P. Jacobs, and V. Cnudde, *Mater Charact* 88, 86 <https://doi.org/10.1016/j.matchar.2013.12.007> (2014).
20. V. Cnudde, J.P. Cnudde, C. Dupuis, and P.J.S. Jacobs, *Mater Charact* 53(2–4), 259 <https://doi.org/10.1016/j.matchar.2004.08.011> (2004).
21. O. Popov, I. Talovina, H. Lieberwirth, and A. Duriagina, *Minerals* 10(2), 129 <https://doi.org/10.3390/min10020129> (2020).
22. Y. Zhao, G. Zhu, S. Liu, Y. Wang, and C. Zhang, *Transp. Porous Media* 128, 653 <https://doi.org/10.1007/s11242-019-01264-4> (2019).
23. H. Kurmus and A. Mohajerani, *Constr. Build. Mater.* 283, 122755 <https://doi.org/10.1016/j.conbuildmat.2021.122755> (2021).
24. E.N. Landis, T. Zhang, E.N. Nagy, G. Nagy, and W.R. Franklin, *Mater. Struct.* 40, 357 <https://doi.org/10.1617/s11527-006-9145-5> (2007).
25. J.M. Hausherr, W. Krenkel, F. Fischer, and V. Altstadt, *Int. J. Appl. Ceram. Technol.* 7(3), 361 <https://doi.org/10.1111/j.1744-7402.2009.02449.x> (2010).
26. A.M. Soltan, H. Pöllmann, R. Kaden, A. König, F.A. El-Raouf, M. Eltahir, and M. Serry, *J. Eur. Ceram. Soc.* 35, 4573 <https://doi.org/10.1016/j.jeurceramsoc.2015.08.018> (2015).
27. N.J. Smith-Gray, J.M. Bussey, and J.S. McCloy, *J. Am. Ceram. Soc.* 195, 7760 <https://doi.org/10.1111/jace.18706> (2022).
28. J. Vaarno, J. Pitkälä, T. Ahokainen, and A. Jokilaakso, *Appl. Mathemat. Modell.* 22(11), 907 (1998).
29. J. Kapusta, *JOM* 56(7), 21 (2004).
30. V. Saari, E. Peuraniemi, and J. Järvi. An update of Boliden Harjavalta copper smelter, In: *The Igor Wilkomirsky Symposium on Pyrometallurgy*, IIMCh, Santiago, Chile, 813 (2022).
31. A. Gheribi, M. des Roches, and P. Chartrand, *J. Non-Cryst. Solids* 505, 154 <https://doi.org/10.1016/j.jnoncrysol.2018.10.006> (2019).
32. P. Hermanek and S. Carmignato, *Case Stud. Nondestruct. Test. Eval.* 6, 122 <https://doi.org/10.1016/j.csndt.2016.05.003> (2016).
33. P. Hermanek and S. Carmignato, *Precis. Eng.* 49, 377 <https://doi.org/10.1016/j.precisioneng.2017.03.007> (2017).
34. D. Chibwe, G. Akdogan, G. Bezuidenhout, J. Kapusta, S. Bradshaw, J. Eksteen, and J.S.A. Inst, *Mining Metall.* 115(5), 349 (2015).
35. M. Mäkipää and P. Taskinen, *Scand. J. Metall.* 9, 273 (1980).